Numerical and Experimental Study of Internal Flow Field for a Carbon Fiber Tow Pneumatic Spreader

J.C. CHEN and C.G. CHAO

In this study, a three-dimensional (3-D) mathematical model of a fiber pneumatic spreader was successfully developed in the physical phenomena of the internal flow field by a far-field treatment at boundary conditions. The 3-D numerical analysis was carried out on incompressible fluid flows in the pneumatic spreader by using finite volume method combined with the k-ε turbulence model which solves Reynolds-averaged Naiver–Stokes equations. Characteristics of the flow field in the spreader at different service conditions are investigated by velocity and pressure distributions. Comparisons of numerical results with measured velocity and pressure distributions were made to determine the accuracy of the employed method. A good agreement was found in both qualitative and quantitative analysis. Fibers were spread on 1:1-scale model of the pneumatic spreader at various fiber transporting rates and air flow rates. Photography techniques were simultaneously used to record the procedures of fibers spread. The carbon fiber tow was easily spread out at service conditions. The performance was better than prior studies in one-dimensional orifice formulation. The results revealed details of the fiber spreading processes. Agreement among those results validated the assumptions inherent to the computational calculation and gave confidence to more complex geometries as well as flow fields. In other words, the use of numerical analysis in the internal flow field was useful for the fiber pneumatic spreader design.

I. INTRODUCTION

OVER the years, carbon fibers have been considered as one of the most important reinforcements for aluminum and its alloy to fabricate advanced composite materials. The carbon fiber (CF) reinforcement/aluminum (Al) matrix composites are of great interest because of their high specific strength and stiffness, low coefficient of thermal expansion, and high thermal/electric conductivity. Therefore, CF/Al composites have the most potential application as structural and functional materials in future. The primary concern in achieving the potential has been the difficulties experienced in combining Al with continuous fiber tows and the chemical reaction at the interface between CF and Al.

The interface plays a most vital role in the overall performance of the composite materials. Improper wetting and chemical reaction occuring at the interface during synthesis or under service conditions can degrade the mechanical properties of the composites.[1–11] Certain coatings can promote the wettability between CF filaments and Al as well as prevent the molten aluminum coming into direct contact with carbon; thus, the chemical reaction can be eliminated. Many methods have been proposed for the preparation of metallic or nonmetallic coated carbon fiber tow.[9,12–15] However, the observed variation in the coating is mainly attributed to nonuniform activation on the surface of the fibers prior to deposition. The nonuniform activation is caused by the compact carbon filaments. Abraham et.al.,[12] Bobka and Lowell,[16] and Clark et al.[17] reported that the oxidation treatment led to a nonuniform etching of the fibers, while carbon fiber tows were treated by oxygen to modify the surface of the filaments. Therefore, the outer filaments are strongly attacked, while those in the interior of the bundle are hardly attacked.

Some variations in the coating techniques of carbon fiber tows have been developed. Ceramic coatings (SiC, TiC, TiB$_2$) or functional gradient coatings (C/SiC/Si) were deposited by chemical vapor deposition (CVD) on carbon filaments for CF/Al composites; however, similar results—that fiber and composite strength decrease with coating thickness and the variations of coating thickness in carbon fiber tow are obvious.—were found[2,7,9] The main problem still exists, which comes from the different treatment between the outer and the interior filaments due to the carbon fiber tows containing thousands of filaments, in spite of the deposition technologies and the deposited materials developed. Therefore, if the carbon fibers are separated uniformly, it is advantageous for the improvement of mechanical properties.[18]

Processes and an apparatus were developed for pneumatically spreading graphite or other carbon filaments from a tow bundle to form a sheet or a ribbon in which the filaments were maintained in parallel.[19–22] The spread filaments can be bonded together in the form of the tape, impregnating any of the well-known resins or thermoplastic polymers, which can be cured or molded under heat and pressure. The key component in the pneumatic spreading system is the spreader, as shown in Figure 1. The carbon fiber tow is comprised of thousands of filaments and the carbon filaments are interacted with air in the spreader.

Baucom and Marchello[22] were the first to tackle the design of a pneumatic spreader; they modeled a single fiber suspended in air under both a pressure drop and tow tension and derived a formulation from the orifice equation to predict the fiber tow spread angle in the spreader. It is suggested that the tow spread may be correlated as a function of fiber tension and pressure drop. Comparisons of the experimental data for a 12 k tow (containing 12,000 filaments) with the

J.C. CHEN, Postdoctoral Candidate, and C.G. CHAO, Professor, are with the Institute of Materials Science and Engineering, National Chiao-Tung University, His-Chu, Taiwan 300, Republic of China.
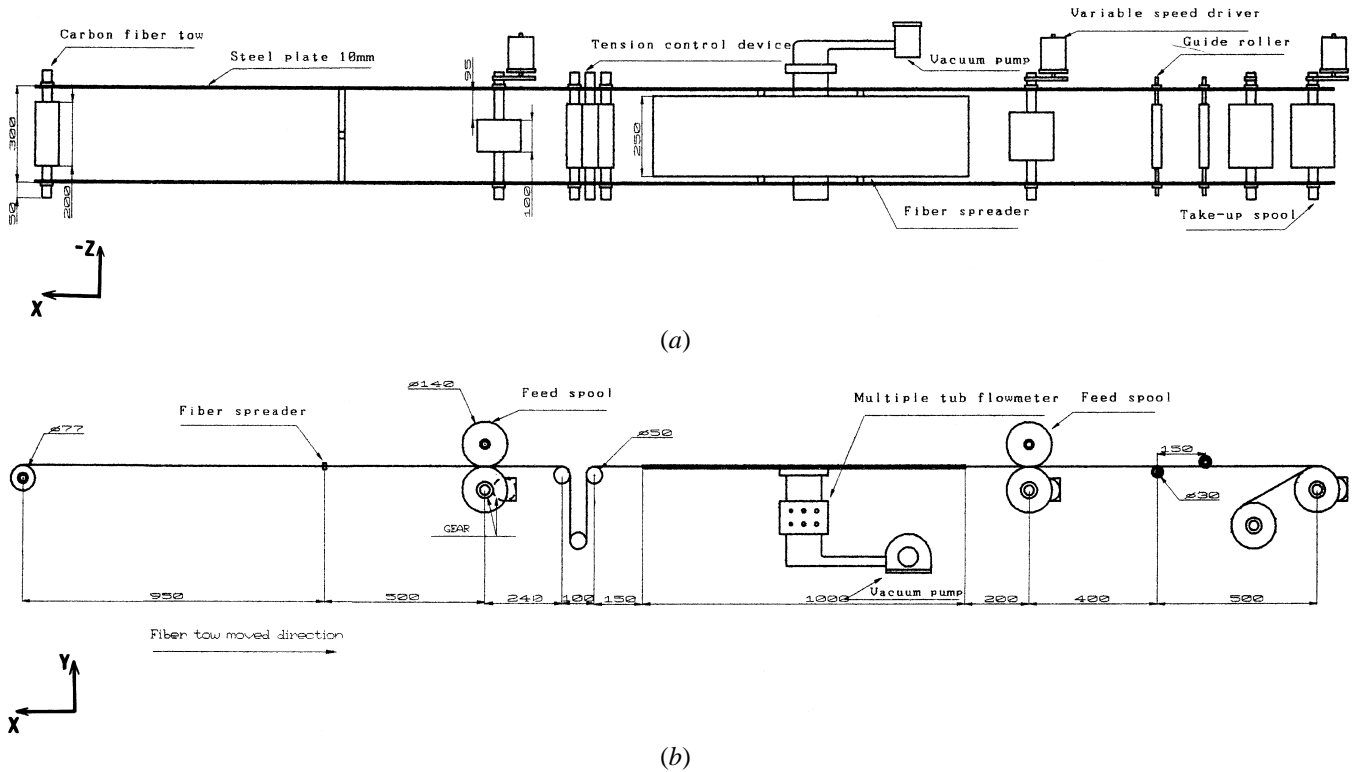Manuscript submitted April 3, 2000.

(a)

(b)

Fig. 1—Schematic of the experimental setup for spreading carbon fiber tow: (a) top view and (b) side view.

single fiber prediction showed that the results were not satisfied because the flow field was too complicated.

None of the previous works investigated the internal flow patterns in qualitative and quantitative analysis about the spreader. Therefore, the exact flow field of the spreader is still unknown. The objective of the present study is to establish a three-dimensional (3-D) mathematical model of the spreader by operating a numerical technique of far-field treatment and to provide a 3-D numerical flow visualization, which reveals velocity fields, pressure distributions, streamlines, and useful flow patterns. The flow patterns contribute to understanding the detail flow field in the physical model, and then help us to develop a new efficient spreader. Finally, a pneumatic spreading system is constructed. In this model system, carbon fiber sheet can be prepared from fiber tow. Meanwhile, photography is used to record the carbon fiber tow spreading process. The spreading mechanism of the carbon filaments is also investigated by combing numerical simulation and experimental analysis.

II. GOVERNING EQUATIONS AND TURBULENCE MODEL

The incompressible and isothermal Reynolds-averaged Navier–Stokes equations are

$$\frac{\partial u_j}{\partial x_j} = 0$$

$$\frac{\partial u_i}{\partial t} + \frac{\partial u_i u_i}{\partial x_i} + \frac{1}{\rho}\frac{\partial p}{\partial x_j} + \frac{\partial}{\partial x_j}\left(\overline{u'_i u'_j}\right)$$

$$- \frac{\partial}{\partial x_j}\left[\nu\left(\frac{\partial u_i}{\partial x_j} + \frac{\partial u_j}{\partial x_i}\right)\right] = 0, \, i, j = 1, 2, 3$$

where u_j is the velocity, p is the pressure, ρ is the constant density, and ν is the molecular kinematic viscosity. The u_i, u_j are the fluctuation parts of the velocity u_i and u_j; and $\overline{u'_i u'_j}$ is the Reynolds stress tensor, which can be modeled by the eddy viscosity hypothesis:

$$\overline{u'_i u'_j} = \check{\tau}_{ij}$$

$$= \frac{1}{\rho}\,\hat{\tau}_{ij}$$

$$= \frac{2}{3}\,\delta_{ij}k - \frac{2}{3}\,\nu_T\,\nabla\cdot u_i\delta_{ij} + \nu_T\,(\nabla u_i + (\nabla u_i)^T)$$

Here, $k = (1/2)\,\overline{u}^2$ is the turbulent kinetic energy, and ν_T is the eddy viscosity. They have to be prescribed by a turbulent model.

The generic k-ε model can be described as [24]

$$\rho\frac{\partial k}{\partial t} + \rho\nabla\cdot(u_i k) = \nabla\cdot((\nu + \sigma_k\nu_T)\nabla k) + \check{\tau}_{ij}\nabla\cdot u_i - \rho\varepsilon$$

$$\rho\frac{\partial\varepsilon}{\partial t} + \nabla\cdot(u_i\varepsilon) = \nabla\cdot((\nu + \sigma_\varepsilon\nu_T)\nabla\varepsilon)$$

$$+ c_1\varepsilon/k\check{\tau}_{ij}\nabla\cdot u_i - c_2\rho\frac{\varepsilon^2}{k}$$

where

Table I. Model Constants Employed in the Computation

c_1	c_2	c_μ	σ_k	σ_ε
1.44	1.92	0.09	1	2.9076

$$\sigma_k = \frac{k^2}{(c_2 - c_1)\sqrt{c_\mu}}$$

where k (Von Karman constant) = 0.4187

The eddy viscosity is calculated from

$$\nu_T = c_\mu \rho \frac{k^2}{\varepsilon}$$

where σ_k and σ_ϵ are the turbulent Prandtl number for k and ε, respectively, and c_1, c_2, and c_μ are the empirical coefficients.[25]

The set of model constants employed is summarized in Table I.

III. BOUNDARY FITTED COORDINATE AND GRID GENERATION

In fact, the geometry of a spreader is too complex to be described by using natural analytic coordinates such as cylindrical coordinates, spherical coordinates, or bipolar coordinates. In this case, the coordinate transformation must be given numerically. There is now extensive literature on the numerical generation of boundary fitted grids.[23,25] Boundary fitted coordinates extend the capabilities of finite difference methods to deal with complex geometry. The basic ideal is to use a curvilinear coordinate transformation, mapping the complex flow domain in physical space to a simple flow domain in computational space. In other words, the Cartesian coordinate system $(x^i) = (x,y,z)$ in the physical domain is replaced by a curvilinear coordinate system $(\xi^i) = (\xi,\eta,\zeta)$ such that boundaries of the flow domain correspond to the surface.

The equations are discretized with respect to the computational space coordinate. Boundary conditions may be implemented naturally in the rectangular computational domain. However, the expense of making the partial differential equations would be higher due to the nonlinear coordination transformation, and a great deal of memory is wasted because of the necessity of designating a large proportion of the grid as solid. The multiblock approach was used in order to maximize computational efficiency and to save memory.[25]

The concept of the multiblock grid is the solution domain, which is divided into subdomains. Each subdomain has its associated subgrid, or block. In multiblock grids, data are transferred from one block to another using a generalization of the periodic boundary condition. The blocks are arranged to overlap such that a boundary surface of one block is situated in the interior of another. After each iteration, the value of variables on the boundary of the first block must cross a boundary surface of the second block; values of variables on this boundary surface can be updated using interior values from the first block.

As shown in Figure 2(a), the geometry of the 3-D spreader model was defined first in a physical space (x, y, z). Because of the symmetry in the vertical plane (x-y plane), to reduce
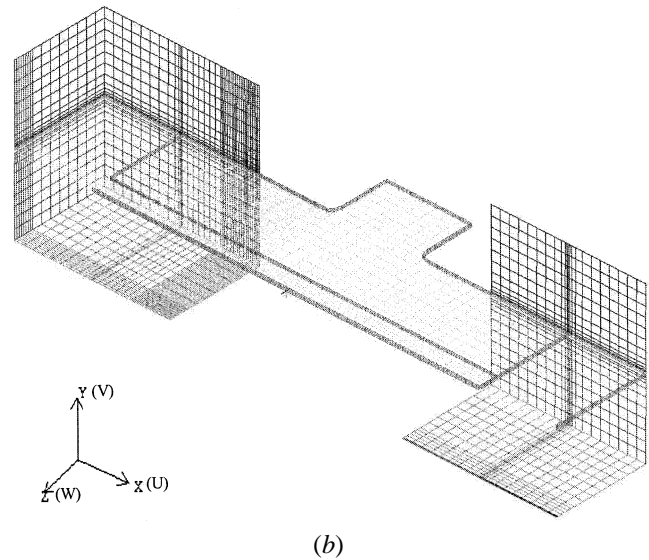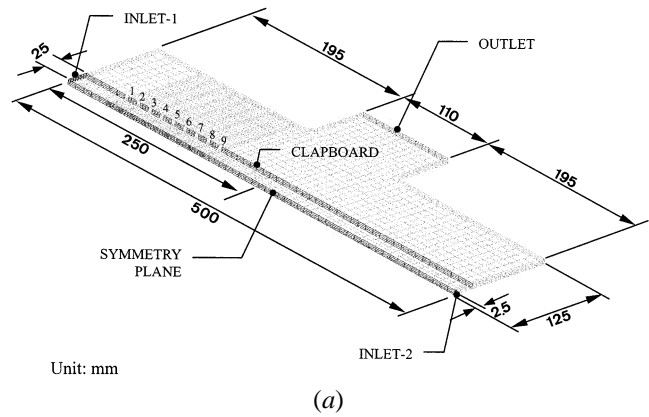

(a)

(b)

Fig. 2—(a) A three-dimensional mathematical model of the pneumatic spreader in a isometric view. (b) A perspective of a far-field treatment by multi block technique in real space (U, V, and W are the velocity components).

computer time, only half of the geometry was simulated. In most simulation work, the boundary conditions at inlets were used to a uniform velocity, which was quoted from measured data, or to an ambient pressure for an internal flow field. In the present study, the inlet velocity was unknown. It was difficult to measure for a sudden contraction case. Therefore, we considered the realistic status as the characterization of the fluid flow in the far field. Thus, the computation domain was extended along x direction and y directions as Figure 2(b) illustrates (a perspective view).

The blocks were built on each side of a spreader model. Therefore, the boundary conditions at the outer surface of each block could be specified by atmospheric pressure (101,300 Pa), and the computation of the flow field was executed from the external flow field to the internal flow field. The grid employed was structured and orthogonal curvilinear. The number of nodes and elements were 137,800 and 129,600 in the fluid domain, respectively. A grid convergence study was performed to ensure that the resolution of this mesh was adequate. Doubling the number of nodes changed the solution by less than 0.01 pct.

IV. COMPUTATIONAL DETAILS

A. *Boundary Conditions*

Quite a bit of literature discussed and stressed the importance of specification of the inlet boundary conditions in the computation of turbulent flows. Sturgess *et. al.* [26] showed that the numerical simulations of flows were highly sensitive to the assumptions made for inlet boundary conditions. Choice of the computational grid was also important. They concluded that overall accuracy of the simulation is determined by assumed boundary conditions and choice of grid. Eaton and Johnston[27] cited that a backward-facing step flow is affected by inlet boundary conditions. They suggested that accurate specification for the inlet boundary conditions including mean velocity and turbulence details is essential to correctly describe the downstream flow field. The boundary conditions employed were as follows.

(1) Symmetry plane

$$V = W = 0$$

$$\frac{\partial U}{\partial x} = 0, \frac{\partial \phi}{\partial x} = 0$$

where

$$\phi = k, \varepsilon, \text{ and } p$$

(2) Pressure boundaries

In the mathematical grid, the computational domains were extended so that the pressure boundaries could be easily created and specified on the surfaces of the blocks as the inlet boundary conditions, as shown in Figure 2(b). For the surfaces sufficiently far downstream, fixed values of all variables could be specified at pressure boundaries.

$$p = 101,300 \text{ (Pa)} \qquad \text{(atmospheric condition)}$$

$$U = V = W = 0 \qquad \text{(free stream)}$$

(3) Outlet

Static pressure was introduced at the outlet location to model outflow boundary. For observing the flow field in the 3-D spreader model, various static pressure conditions were used for computation, including 101,100, 101,200, and 101,250 Pa, respectively. It was useful to predict the experimental condition and make a comparison of velocities computed by various pressure and measured data.

(4) Walls

The boundary wall was fixed, and a no-slip condition was imposed on all velocity components. Many variables varied rapidly in the near wall regions of the flow, instead of using extremely fine grids in these regions; therefore, their behavior was specified with wall functions. The wall functions were illustrated below by considering the flow in a fully developed boundary layer over a stationary wall.[24] Near the wall ($y = d$), it was found that the wall shear stress τ is related to the turbulence kinetic energy by

$$\tau^2 = c_\mu \rho^2 k^2$$

A new quantity is defined such that

$$\tau_k = \rho c_\mu^{1/2} k$$

This may be used to define scaled variables

$$u^+ = -\frac{(\rho \tau_k)^{1/2}}{\tau} u$$

and

$$y^+ = -\frac{(\rho \tau_k)^{1/2}}{\mu} (d - y)$$

The scaled velocity component parallel to the wall and in the x directions is

$$u^+ = \begin{cases} y^+, \text{ for } y^+ < y_0^+ \\ \frac{1}{k} \log (Ey^+), \text{ for } y^+ > y_0^+ \end{cases}$$

where log is a natural logarithm.

The crossover point y_0^+ between the viscous sublayer and the logarithmic region is the upper root of

$$y_0^+ = \frac{1}{k} \log (Ey_0^+)$$

The equation for the turbulence kinetic energy k is solved in the control volume immediately adjacent to the wall. From the value of the wall shear stress, τ can be obtained. The turbulence dissipation is obtained from the turbulence kinetic energy through the relation

$$\varepsilon = \frac{c_\mu^{3/4} k^{3/2}}{k(d - y)}$$

B. *Discretization and Computational Procedures*

Discretization has been carried out using the finite volume method. The governing equations were integrated over the control volume and reduced to algebraic equations, which followed conservation laws. Once a grid of points was set up over the field, all the unknown variables were stored in the certain of the computational cells. In order to avoid pressure-velocity decoupling problems, arising from the fact that pressure and velocity were calculated in the same location, the convection flux through each cell faces was calculated by using the modification first proposed by Rhie and Chow,[28] extended here for a multiblock grid. The major achievement of this approach is that it provides a prescription for implementing the standard primitive variable algorithms such as SIMPLE and SIMPLEC using a non-staggered grid. The feature of the prescription is that the velocity needed for the calculation of the connective flux through a cell face is not obtained from a linear interpolation of the adjacent cells' velocities. However, the velocity is modified to be directly linked to the two adjacent pressure nodes. Following this procedure, the SIMPLE algorithm was used as a pressure-correction method,[29] in order to derive the pressure equation from the continuity equation.

The treatment of the convection term determines the accuracy of the solutions of the model equations. The CCCT scheme was used for the discretization of convective fluxes. The CCCT scheme is a modification of the quadratic upwind differencing scheme (QUICK), which is an upwind scheme with third-order accuracy and can suffer from nonphysical overshoots in its solutions.[28] The diffusion terms were discretized in space using a second-order centered difference scheme. The set of linearized difference equations, after the discretization of the conservation equations, were passed to

a simultaneous linear equation solver, which used an iterative solution method. The STONE method was available for this purpose and was very efficient in a vector computer. In this work, since the transient evolution was not of interest, the time-stepping scheme could be optimized for faster convergence. Acceleration techniques such as false time-step were applied.[25]

Therefore, a typical simulation of the 3-D model on the base mesh required 300 MB of memory, and consumed a total CPU time of 7.237×10^4 seconds. The program was executed on a vector computer, CRAYJ916* supercomputer,

---

---

with eight 100 MHz processors and 1 GB main system RAM.

V. EXPERIMENT

A. *Experimental Setup*

Experiments were conducted using the setup shown schematically in Figure 1. The main elements were comprised in a sequence of the tow feed spool, tension control device, pneumatic tow spreader, vacuum pump, and take-up spool. The fibers from the carbon fiber tow containing 12,000 filaments were passed through a fiber guide into a first friction roller. The first roller was synchronized with the second friction roller at a constant rate of speed. The two rollers were controlled by a variable speed driver. Hence, the fibers between the two rollers, which were subsequently spread in the pneumatic spreader, remained in a low tensional state that was given by the tension control device. For the air flow rate in the pneumatic spreader, the vacuum pump sucked air and gave a stable control of flow rate, which was measured by a multiple tube flow meter and a precision pressure controller. After the fibers spread and left the second roller, the fibers were taken up by a take-up system.

B. *Experimental Techniques*

The design of the spreader must satisfy several interacting requirements. Although high air velocity resulting drag force to fibers is desirable, streamwise velocity is constrained by the need to avoid circulation and excessive agitation of the airflow. Agitation can cause fibers to become entangled, which makes fiber spread difficult and damages fibers. This is the first 3-D mathematical model of a pneumatic spreader. Therefore, the height of the spreader and the distance from the symmetry plane to the clapboard were the two design parameters in the spreader. The spreader formed by PAN (polyacrylonitrile) pieces, which were transparent allowing the spread procedure of carbon fibers to be photographed for subsequent qualitative comparison with computational results, had a through-length 500 mm in x-direction, as shown in Figure 2(a). The half-width of the spreader was one-fourth (125 mm) of the length.

The projecting part connected to a vacuum pump had the width 80 mm in the z direction and a length of 110 mm in the x direction. The fiber entrance named inlet-2 was 2.5 mm in half-width. The fiber exit named inlet-1 had a 25-mm half-width selected as the final fiber spread width. The clapboard contained nine slots, which were parallel to the symmetry plane.

Each slot was 5-mm wide and 10 mm apart; the first slot was behind the inlet-1, which was 50-mm long. To simplify the computational problem, the distance from the symmetry plane to the clapboard was set at three different dimensions, 105, 70, and 25 mm. Similarly, the height of the spreader was also set at three different dimensions: 20, 10, and 5 mm. They were explored by using numerical simulation at various boundary conditions, whereas the computational results were useful in understanding how air fluid interacted with carbon fibers.

According to the simulate results, the spreader would be modified and spread experiments would be undertaken to test the applicability of the 3-D mathematical model. First, the downstream pressures and velocities near the outlet were measured by a precision pressure controller and digital micromanometer, under various flow rates without carbon fiber tow, and the velocities were compared with the calculated data to confirm the accuracy. Experiments of fiber spread were executed at various fiber transporting rates and air flow rates. Photography techniques were used to record the processes of fiber spread. The photographs were taken from the top view. Five Nikon FM2 cameras were used and each was fitted with a 52-mm lens. The single-frame photographs were taken with shutter speeds of 1/15 to 1/60 seconds, so that the images showed how fiber was spread and moved in the pneumatic spreader.

VI. RESULTS AND DISCUSSION

To study the geometry effect of the spreader, the simulation was conducted using height with three different dimensions, 20, 10, and 5 mm. Hence, there were three different cross-sectional areas: 500 and 100 mm^2 at inlet-1 and inlet-2, for case 1, respectively; 250 mm^2 at inlet-1 and 50 mm^2 at inlet-2 for case 2; and 125 mm^2 at inlet-1 and 25 mm^2 at inlet-2 for case 3. The boundary conditions using pressure drop (0.275 psi) between upstream and downstream were given by Baucom *et al.* It was found the pressure dropped abruptly as the cross-sectional area decreased, which caused a significant increment in air flow velocity at inlet-1 from 21.6 m/s for case 1 up to 44 m/s for case 3. The velocity increase is inversely proportional to the cross-sectional area, while the pressure drop is related to the square of the flow velocity. The pressure drop is also inversely proportional to the cross section of the fiber flow outlet (inlet-1). Hence, the spreader model was set with 5 mm in height.

The other parameter, the distance from the symmetry plane to the clapboard, was also set with three dimensions 105, 70, and 25 mm. The flow field for the distance 25 mm was taken as an example shown in Figure 3. The streamlines were plotted at the central plane ($y = 25$ mm) of the mathematical model. There were three circulations in the spreader.

(1) The air was sucked into the spreader and then the air was accelerated due to sudden contraction at inlet-2. Therefore, the circulation zone was formed by fluid viscosity and drag.
(2) The air flow entered inlet-1 and passed through the nine slots on the clapboard; thus, there were two circulation zones behind the clapboard.

However, the main interest of the present investigation was the flow field from the symmetry plane to the clapboard. While the distance increased from 25 to 105 mm, the circulation zone would increase at inlet-2 and appear at inlet-1; it
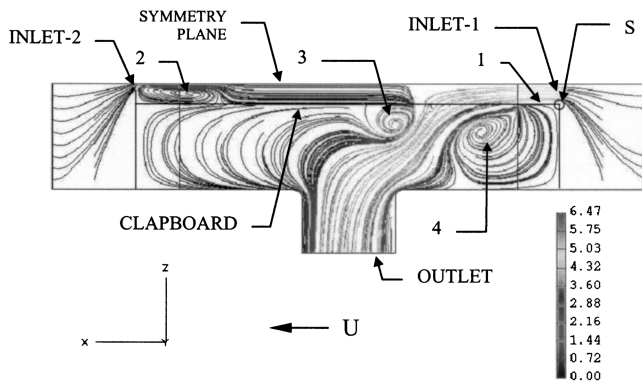
Fig. 3—A complete view of streamlines at the central plane ($y = 2.5$ mm) under pressure drop 50 Pa between far-field pressure boundary and outlet pressure boundary.
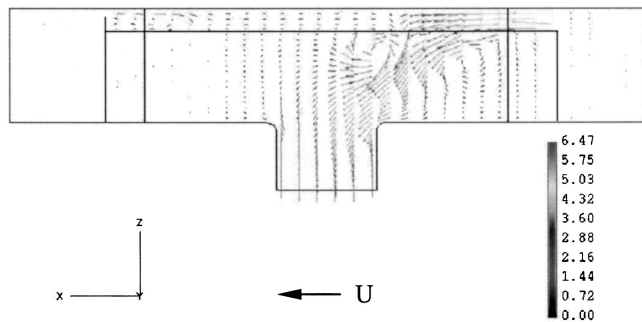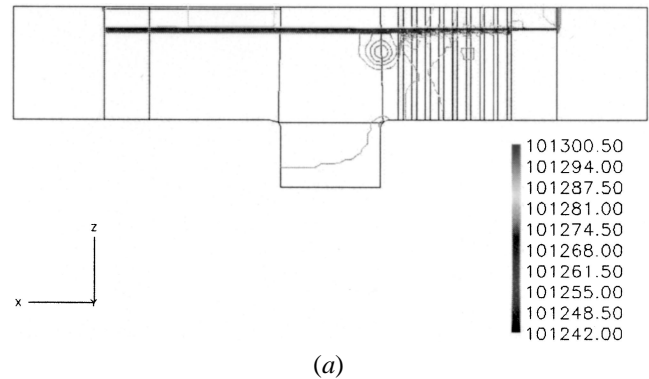

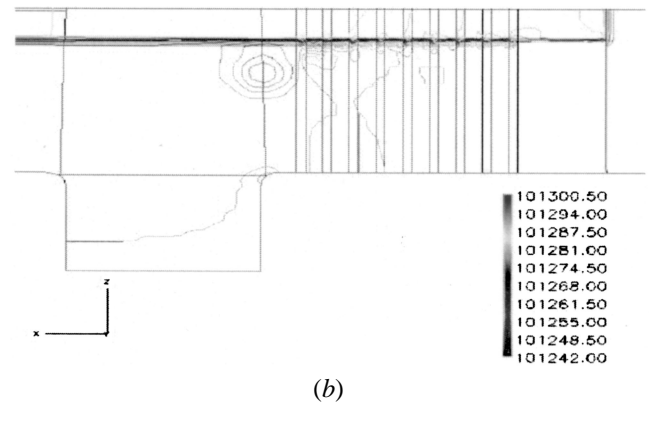Fig. 4—Velocity-vector representation of the flow field in Fig. 3.

(a)

(b)

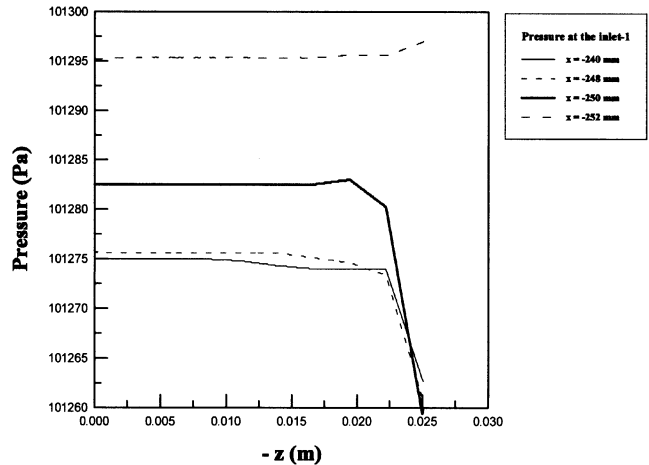Fig. 5—Pressure contour under pressure drop 50 Pa: (a) a complete view and (b) a close-up view.

Fig. 6—Calculated pressure distributions at the inside and outside of the inlet-1 (inside of the inlet-1: ———, -----; inlet plane: ———; outside of the inlet-1: – –).

makes fiber spread difficult. Since there was a slow velocity in the circulation zone, the fibers were hard to drag by air flow. In order to avoid the circulation zone, the distance from the symmetry plane to the clapboard was set with 25 mm. To understand the flow field under various boundary conditions, three cases with different pressure boundary conditions at the outlet surface were examined with the two parameters in the model. For the three cases, the pressures were 101,100, 101,200, and 101,250 Pa, respectively; however, the calculated flow fields were all very similar, so only the flow field for case 3 (101,250 Pa) was shown in Figures 3 and 4.

A velocity vector showed the main characteristics of the air flow. The varieties of flow velocity appeared at inlet-1 and slots, since the cross-sectional area decreased. However, there was a stable flow downstream around the outlet. The velocity of air flow showed an extremely small difference between inlet-1 and inlet-2. It is well known that $Q = \rho UA$, where Q is the flux, ρ is the fluid density, U is the fluid velocity, and A is the cross-sectional area of inlet. Furthermore, the flux at inlet-1 was 10 times larger than that at inlet-2, and the slots on the clapboard were close to inlet-1; therefore, the main variations in air flow would occur at inlet-1 nearby, so we concentrated the discussion in the region from inlet-1 to the slots.

A complete view of the pressure contour was seen in Figure 5(a), which showed the low pressure distributed at the slots. A close-up view of the pressure contour in the vicinity of inlet-1 was shown in Figure 5(b). The detail pressure distribution was calculated and had a slight difference of about 30 Pa compared with the far-field pressure of

the spreader, but an evident difference was presented in case 1 (101,100 Pa). Therefore, if the simulation was in a low speed flow field, we could remove the outward block and take an ambient pressure boundary in the vicinity of inlet-1 and inlet-2 to save the CPU time. In other words, the treatment of far-field boundary conditions has good calculated results at high speed flow field. Figure 6 showed that the calculated pressure distributions were at the inside and outside of inlet-1. It was clear that the pressure dropped
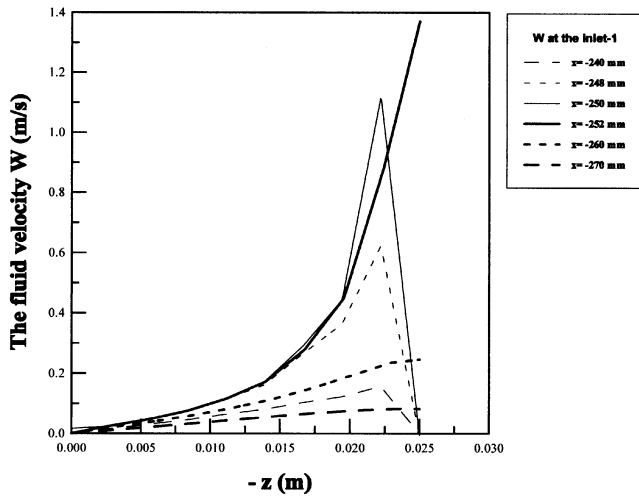
Fig. 7—Calculated W-velocity components from symmetry plane to the clapboard along x-direction in the vicinity of inlet-1 (inside of the inlet-1:-----, --; inlet plane: ————; outside of the inlet-1: ———, -----, --).
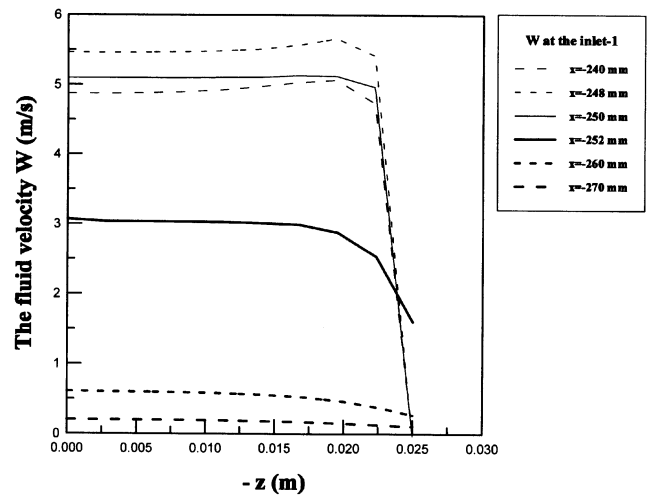

Fig. 9—Calculated U-velocity components from symmetry plane to the clapboard along x-direction in the vicinity of inlet-1.
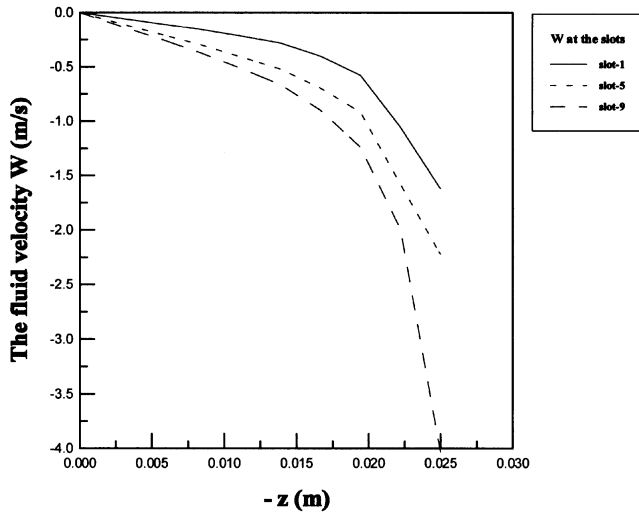

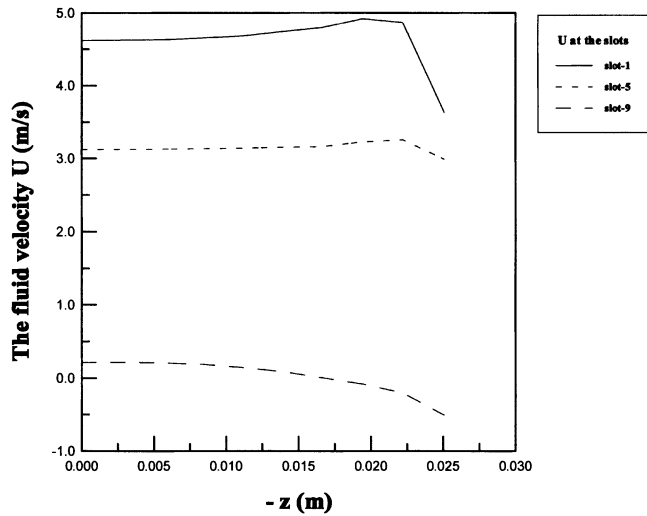Fig. 8—Calculated W-velocity distributions from symmetry plane to the clapboard in front of slots 1, 5, and 9.

Fig. 10—Calculated U-velocity distributions from symmetry plane to the clapboard in front of slots 1, 5, and 9.

abruptly due to a sudden contraction. There was some difference about 20 Pa between the inside and outside of inlet-1. Additionally, a narrow low pressure zone (z = 0.022 to 0.025 m) formed near the clapboard because the air flow passed through the separation location S; hence, air flow separation generated. Air could not enter this zone near the clapboard, so it was thin and there was no air flow; thus, pressure dropped.

The distribution of the lateral velocity W was reducing with the distance Z approaching the symmetry plane. Inversely, the more air flowed into the inner location, the more velocity W increased. Above all, much variation in the velocity W existed behind the slots. The calculated velocity W in the vicinity of inlet-1 was shown in Figure 7. There was a larger velocity at the outside of inlet-1 near the clapboard, while the air was sucked into the spreader. It should be noted that the treatment of far-field boundary could facilitate the calculation at the cross section of inlet-1. Generally, the calculation of the internal flow field set a uniform inflow

at the inlet of a fluid; therefore, the numerical error could not be avoidable.

The W-velocity component at slots 1, 5, and 9 was calculated and presented in Figure 8. Each curve represented the velocity variation of each slot from the symmetry plane.

The physical model was constructed according to the designed parameters. To test the accuracy of the numerical experiment, a series of experimental measurements were made, and a comparison of the calculated velocity with the measurement is presented in the following figures. Figure 12 shows a comparison between computation and measurement of the outlet velocity at the static pressure on the centerline of the outlet. It was found that the computational data were in good agreement with the measured data. Similar trends were observed at the static pressure, 101,200 Pa, as shown in Figure 13.

Theoretically speaking, the converged solution was calculated from upstream to downstream; moreover, the upstream computational results had the same order in numerical error as the downstream. The simulated and measured data were
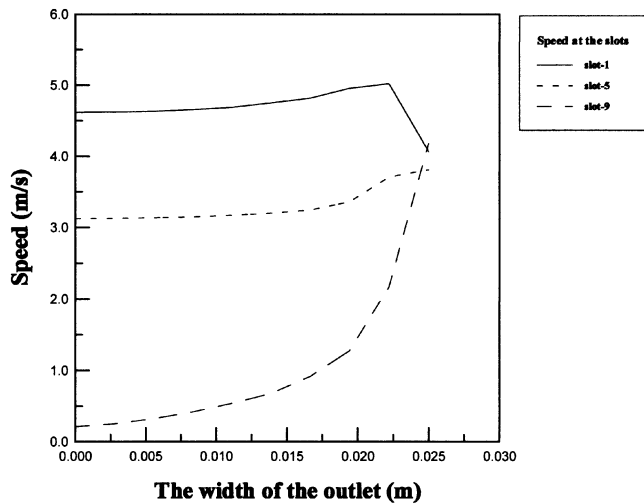
Fig. 11—Calculated speed distributions from symmetry plane to the clapboard in front of slots 1, 5, and 9.
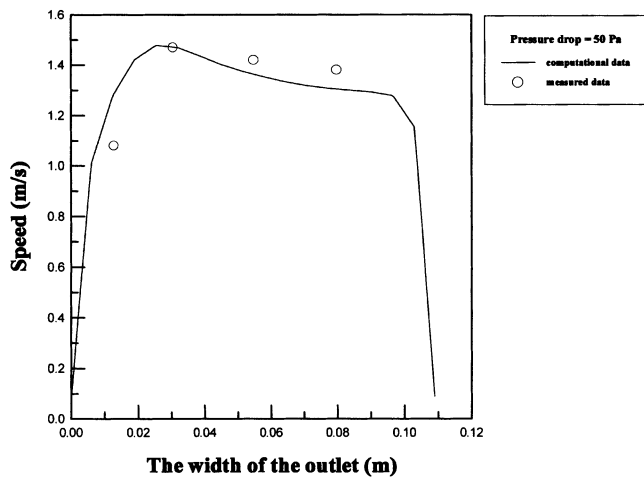

Fig. 12—Comparison of computational and measured speed at outlet under pressure drop 50 Pa.
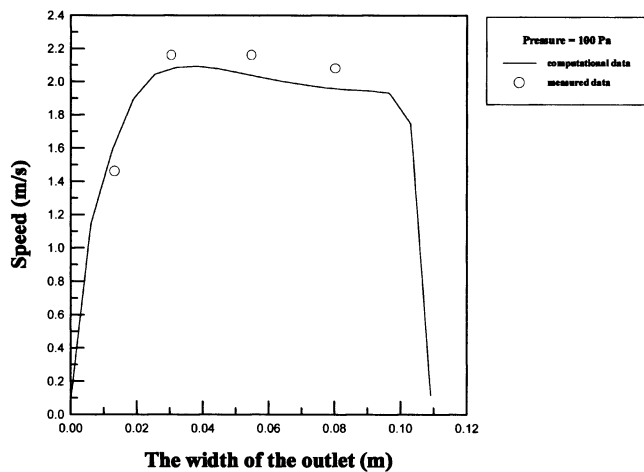

Fig. 13—Comparison of computational and measured speed at outlet under pressure drop 100 Pa.

both qualitatively and quantitatively similar; further, the 3-D computational results can be helpful for designing a pneumatic spreader. Although considering no fiber addition might not be precise enough to lead to an understanding of the interaction of fiber and air flow, the results gave us insight and led to the realization of the 3-D flow field.

The air flux was related to the fluid velocity and pressure in the spreader and was controlled by the flowmeter. They were measured and presented in Figures 14(a) and (b). It was found that the mean mass flow rate was proportional to the mean static pressure and mean static pressure was also linearly increased with mean fluid speed. Similarly, the computational results have the same trend as the measured results. Therefore, the flow field can qualitatively be understood before the fiber spreading experiment is executed.

Figure 15 shows a fiber spreading experiment under $V_F = 7$ m/min and $Q = 90$ L/min, perpendicular to the center of a slot. It was seen that air flowed toward the slots, yielding a slight change in velocity, but the magnitude of the velocity increased abruptly near the slots ($Z = -0.02$ m), since the cross-sectional area was suddenly contracted. The air entered the spreader through inlet-2 and turned toward slot 9; therefore, the W velocity at slot 9 is larger than that at other slots. The air flow was accelerated at the inside of inlet-1 and inlet-2, and the large velocity U was near the symmetry plane. The U-velocity gradually decayed at the inner location, while the air flow turned toward slots on the clapboard (-Z direction).

Figure 9 presented the calculated U-velocity in the vicinity of inlet-1. The U-velocity with an average velocity 0.6 m/s at the outside of inlet-1 ($x = -260$ mm) was accelerated up to an average velocity 5.5 m/s at the inside of inlet-1 ($x = -248$ mm). Moreover, as has been realized by previous discussion, the air flow could not enter the low pressure zone near the clapboard ($Z = -0.22$ m) due to the effect of separation flow. Hence, little air flowed in this zone, so that the U-velocity decayed. The distribution of the U-velocity component from the symmetry plane to the slots was shown in Figure 10. The results indicated that there were smaller U-velocity components at the inner location due to the air flow turned direction. There was a negative U-velocity around slot 9; this was because air flow came from inlet-2. In this investigation, because the V-velocity component was not found, it was found that the flow field was a two-dimensional flow in the spreader.

Figure 11 showed the speed variations in front of slots 1, 5, and 9. The speed was the resultant velocity of U- and W-velocity components. The results indicated that the main air flow come from inlet-1 and there was similar magnitude of speed around where V_F was the fiber transporting velocity and Q was the air mass flow rate. It was seen that the fibers were easily spread, and most fibers were dragged toward the clapboard and concentrated at the clapboard side; the reason for this was that the fluid velocity was fast.

While the conditions were set with $V_F = 7$ m/min and $Q = 70$ L/min, the fibers were spread in width about 20 mm at fiber exit. Fiber tow was spread by axial velocity; however, the axial velocity was not large enough to make fibers move to the location where the lateral W-velocity was larger. However, Baucom et al. argued that air entered through the tow exit and was drawn through the slots on
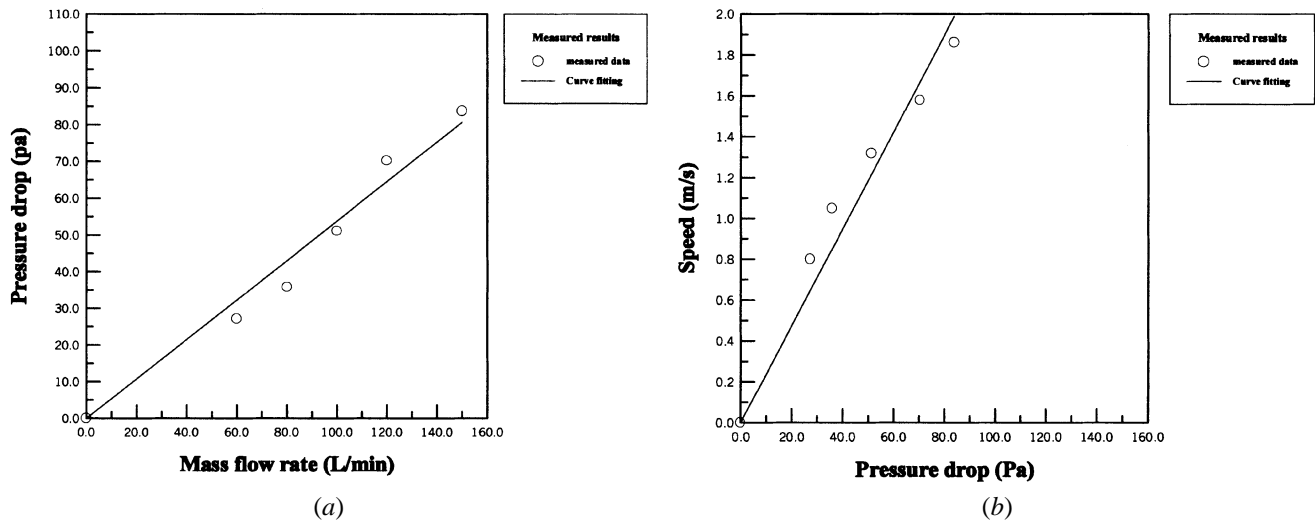
Fig. 14—(*a*) The relations of the experimentally measured mean mass flow rates and pressure drops at outlet. (*b*) The relations of the experimentally measured pressure drops and speeds at outlets.
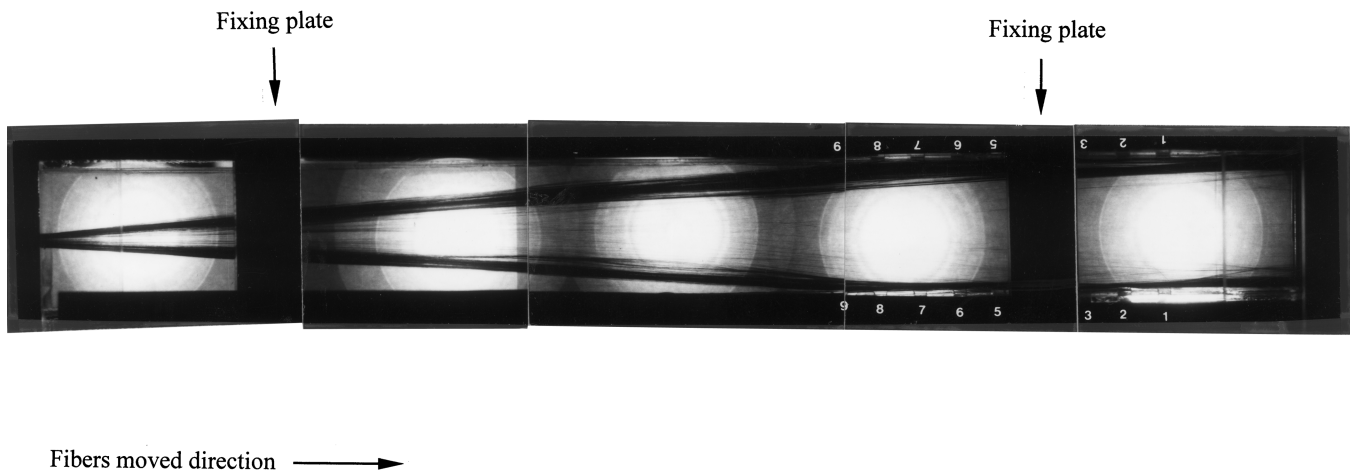

Fig. 15—Photograph of fibers spread experiment under V_F = 7 m/min and Q = 90 L/min.

the clapboard of the expansion section into a vacuum manifold. This cross-flow of air provided drag on the carbon fibers, resulting in tow spread across the pneumatic spreader.

The fiber spread procedure at the condition V_F = 7 m/min and Q = 80 L/min was shown as follows. Figure 16(a) indicates that the fiber tow was transported in the spreader. Initially, the fiber tow was spread out and fluffy at the fiber exit, as shown in Figure 16(b), because there was a maximum axial U-velocity at the exit (inlet-1) due to a sudden contraction and an acceleration of air flow. Sequentially, fibers were gradually spread out, and the partial spread fiber extended to the inner of the spreader about the location of the fifth slot, as shown in Figure 16(c). Futhermore, the spread width at the inner location was slightly larger than that at the fiber exit, because the air flow turned toward the slots. Compared to Figure 8, the air drag was gradually increased. Finally, fibers were dragged toward the clapboard and maintained the width they had when they left the spreader, as shown in Figure 16(d). There were similar spread results on the other conditions, and the fiber spread procedure was all the same. However, Baucom *et al.*

reported that the 12 k tow was spread to a 5.08-cm width at a tow rate of V_F = 3 m/min, and the pressure drop was kept at P = 0.275 psi.

In this study, we proposed an excellent performance and efficiency application for spreading a fiber tow. Additionally, in a continuous fiber spreading procedure, there were three main steps recounted as follows:

(1) the fiber flow was first spread at the fiber exit by the axial air flow;
(2) fibers gradually moved toward the lateral side, and the lateral W-velocity influenced the fiber movement; and
(3) the fibers were closer to the clapboard; as the W-velocity increased, the fibers were dragged toward the clapboard.

The proposed spread procedure was more detailed and quite different from that of Baucom *et al.* Indeed, the 3-D computational results can be helpful for designing a pneumatic spreader. Resigning a pneumatic spreader intends to satisfy various requirements, such as stable flow field, avoiding circulation and vortex, and no abrupt velocity and pressure gradient variations in the spreader.
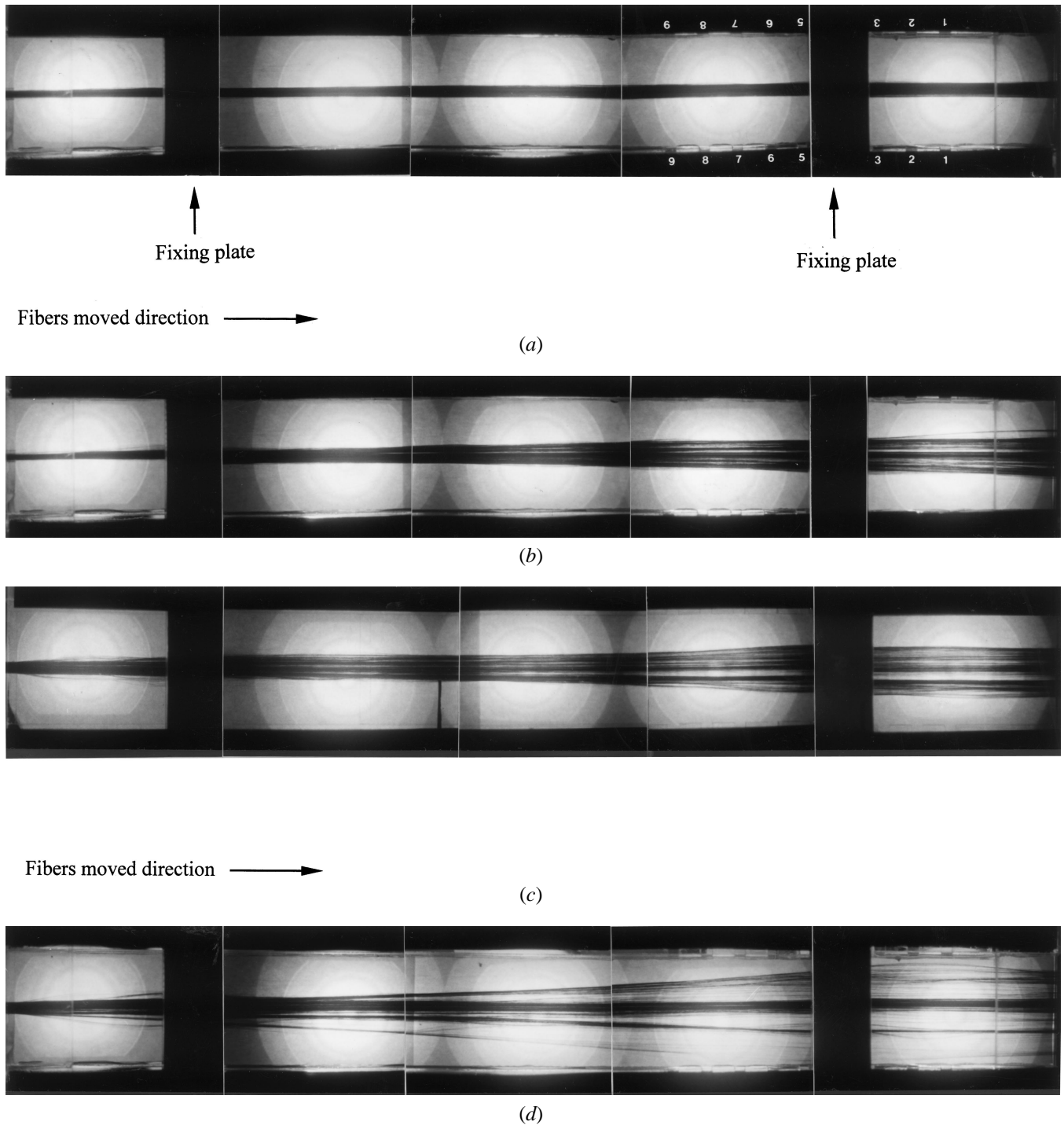
Fig. 16—Photographs of fibers spread experiment under $V_F = 7$ m/min and $Q = 80$ L/min: (*a*) initial state, (*b*) fibers spread to lateral side, (*c*) more fibers moved to lateral side, and (*d*) final state.

Although our simplified simulation without fiber tow may not be precise enough, the results give us a detailed quantitative observation to explore the 3-D flow field, *i.e.*, velocity and pressure distribution. The comparison between the simulated and experimental results clearly shows that the numerical approach reported here can be used to study the pneumatics spreader.

VII. CONCLUSION

This is the first 3-D mathematical model of the fiber spreader and the first time it has been viewed using a photographic technique. The major results and conclusion from this work are summarized as follows.

1. The far-field treatment at the boundary condition by the

multiblock technique, which extends the computational domain to far upstream, can improve the calculated accuracy at the fiber exit (inlet-1) nearby, and it is more useful at large pressure drop conditions.

2. The turbulent k-ε model, which includes incorporation of a wall function, is employed to study the fluid behavior of air flowing through the spreader. The circulation zone and separation flow can be simulated accurately.

3. The simulation results are in excellent agreement with the experimental measurements downstream, and the result can be used to analyze the flow field upstream. Therefore, the designed parameters are determined; the height of the spreader is 5 mm, and the distance from clapboard to symmetric plane is 25 mm.

4. The fiber tow was successfully spread at various conditions, and the performance is better than in prior studies. The optimum and efficient condition in the fiber spreading operation is $V_F = 7$ m/min and $Q = 80$ L/min, and the operating pressure drop is 33 Pa, which is smaller than Baucom and Marchello reported.

5. The fiber spreading procedures are first proposed, and they can help in understanding the spread process and provide the ability to test the design of the pneumatic spreader.

6. The 3-D simulation is successfully combined with experiment for the application of carbon fiber tow spread, and this methodology is often used in the fiber spread process.

NOMENCLATURE

A	cross-sectional area
$c_1, c_2,$ and c_1	empirical coefficient
E	empirical coefficient
k	turbulent kinetic energy
p	pressure
t	time
$\overline{u_i' u_j'}$	Reynolds stress tensor
u_i', u_j'	fluctuation parts of the velocity
u_j	velocity
$\overline{u}$	average velocity
u^+	scaled velocity
U, V, W	velocity components
V_F	fiber transported velocity
x, y, z	Cartesian coordinates
y^+	dimensionless distance

Greek Characters

ε	turbulent dissipation rate
μ_τ	turbulent viscosity
k	Von Karman constant
ξ, ζ, η	curvilinear coordinate
v	molecular kinematic viscosity
v_T	eddy viscosity
ρ	density
σ_K	turbulent Prandtl number for k
σ_ε	turbulent Prandtl number for ε
τ	shear stress
$\tilde{\tau}_{ij}$	Reynolds stress tensor
φ	general variable

Mathematical Operators

∇	del operation
∂	partial derivative

REFERENCES

1. F. Delannay, L. Foryen, and A. Deruyttere: *J. Mater. Sci.*, 1987, vol. 22, pp. 1-16.
2. R.V. Subramanian and A. Nyberg: *J. Mater. Res.*, 1992, vol. 7 (3), pp. 677-88.
3. Li-Min Zhou, Yiu-Wing-Mai, and Caroline Baillie: *J. Mater. Sci.*, 1994, vol. 29, pp. 5541-50.
4. Sunil G. Warrier and Ray Y. Lin: *Scripta Metall. Mater.*, 1993, vol. 29, pp. 1513-18.
5. Zhenhia Xia, Yaohe Zhou, Zhiying Mao, and Baolu Shang: *Metall. Trans. B*, 1992, vol. 23B, pp. 295-302.
6. R. Asthana: *J. Mater. Sci.*, 1998, vol. 33, pp. 1959-80.
7. G. Leonhardt, E. Kieselstein, H. Podlesak, E. Than, and A. Hofman: *Mater. Sci. Eng.*, 1991, vol. A135, pp. 157-60.
8. Andreas Mortensen: *Mater. Sci. Eng.*, 1991, vol. A135, pp. 1-11.
9. J.K. Yu, H.L. Li, and B.L. Shang: *J. Mater. Sci.*, 1994, vol. 29, pp. 2641-47.
10. D. Huda, M.A. El Baradie, and M.S.J. Hashmi: *J. Mater. Processing Technol.*, 1993, vol. 37, pp. 529-41.
11. Feng Wu and Jing Zhu: *Composites Sci. Technol.*, 1997, vol. 57, pp. 661-67.
12. Susan Abraham, B.C. Pai, K.G. Satyanarayana, and V.K. Vaidyan: *J. Mater. Sci.*, 1999, vol. 25, pp. 2839-45.
13. S. Abraham, B.C. Pai, and K.G. Satyanaryana: *J. Mater. Sci.*, 1992, vol. 27, pp. 3479-86.
14. H.M. Cheng, A. Kitahara, S. Akiyama, K. Kobayashi, and B.L. Zhou: *J. Mater. Sci.*, 1992, vol. 27, pp. 3617-23.
15. Yu-Qing Wang and Ben-Liam Zhou: *J. Mater. Processing Technol.*, 1998, vol. 73, pp. 78-81.
16. R.J. Bobka and L.P. Lowell: *Handbook of Composites, vol. 1 - Strong Fibres,* W. Watt, and B. V. Perov, eds., Elsevier Science Publisher B.V., 1985, pp. 579-80.
17. D. Clark, N.J. Wadsworth, and W. Watt: *Handbook of Composites, vol. 1 - Strong Fibres,* W. Watt, and B. V. Perov, eds., Elsevier Science Publisher B.V., 1985, pp. 579-80.
18. Haining Yang, Mingyuan Gu, Weiji Jiang, and Guoding Zhang: *J. Mater. Sci.*, 1996, vol. 31, pp. 1903-07.
19. Clare G. Daniels: U.S. Patent No. 3,873,389, Philco-Ford Corp., Philadelphia, PA, El Toro, CA, Mar. 25, 1975.
20. Paul E. McMahon, Tai-Shung Chung, and Lincoln Ying: U.S. Patent No. 4,871,491, BASF Structural Materials, Inc., Charlotte, N.C., Oct. 3, 1989.
21. John N. Hall: U.S. Patent No. 3,704,485, Hercules Incorporated, Wilmington, DE, Brookside Park, DE, Dec. 5, 1972.
22. Robert M. Baucom and Joseph M. Marchello: *Sampe Q.*, 1990, July, pp. 14-19.
23. J.F. Tompson: *Numerical Grid Generation*, Elsevier, New York, NY, 1982.
24. E.B. Launder and B.D. Spalding: *Mathematical Models of Turbulence*, Academic Press, London, 1972.
25. *CFX-F3D Version 4.1 User Manual*, Harwell Laboratory, Oxfordshire, U.K., 1995, Oct.
26. G.J. Sturgess, S.A. Sayed, and K.R. McManus: *Int. J. Turbo Jet Engines*, 1986, vol. 33, pp. 43-55.
27. J.K. Eaton and J.P. Johnston: *AIAA J.*, 1981, vol. 19 (9), pp. 1093-1100.
28. M.C. Rhie and L.W. Chow: *AIAA J.*, 1983, vol. 21, pp. 1525-32.
29. S.V. Patankar and B.D. Spalding: *Int. J. Heat Mass Transfer*, 1972, vol. 15, pp. 1787-92.